Chemistry Europe
European Chemical Societies Publishing

WILEY VCH

Excellence in Chemistry Research

Announcing our new flagship journal

- Gold Open Access
- Publishing charges waived
- Preprints welcome
- Edited by active scientists

Meet the Editors of *ChemistryEurope*

Luisa De Cola
Università degli Studi di Milano Statale, Italy

Ive Hermans
University of Wisconsin-Madison, USA

Ken Tanaka
Tokyo Institute of Technology, Japan

Chemistry–A European Journal
Research Article
doi.org/10.1002/chem.202202697
Chemistry Europe
European Chemical Societies Publishing
www.chemeurj.org

Photophysics of Anionic Bis(4*H*-imidazolato)Cu^{I} Complexes

Bianca Seidler,[a, b] Jens H. Tran,[a] Julian Hniopek,[a, b, c] Philipp Traber,[a] Helmar Görls,[d] Stefanie Gräfe,[a, c] Michael Schmitt,[a, c] Jürgen Popp,[a, b, c] Martin Schulz,*[a, b] and Benjamin Dietzek-Ivanšić*[a, b, c, e]

Abstract: In this paper, the photophysical behavior of four panchromatically absorbing, homoleptic bis(4*H*-imidazolato)Cu^{I} complexes, with a systematic variation in the electron-withdrawing properties of the imidazolate ligand, were studied by wavelength-dependent time-resolved femtosecond transient absorption spectroscopy. Excitation at 400, 480, and 630 nm populates metal-to-ligand charge transfer, intraligand charge transfer, and mixed-character singlet states. The pump wavelength-dependent transient absorption data were analyzed by a recently established 2D correlation approach. Data analysis revealed that all excitation conditions yield similar excited-state dynamics. Key to the excited-state relaxation is fast, sub-picosecond pseudo-Jahn-Teller distortion, which is accompanied by the relocalization of electron density onto a single ligand from the initially delocalized state at Franck-Condon geometry. Subsequent intersystem crossing to the triplet manifold is followed by a sub-100 ps decay to the ground state. The fast, nonradiative decay is rationalized by the low triplet-state energy as found by DFT calculations, which suggest perspective treatment at the strong coupling limit of the energy gap law.

Introduction

The development of efficient photosensitizers for the transformation of renewable energies[1–9] or artificial photosynthesis[1,2] is an important field of contemporary research.[10] In particular, transition-metal-based photosensitizers are of great interest as light-harvesting units due to the tunability of their optical, electronic, and redox properties.[11–16] Noble-metal-free photosensitizers are required for sustainable photochemistry to replace scarce and expensive transition metals, such as ruthenium, iridium, or platinum.[1,3,7,9,11,13,15–21] An important requirement for a photosensitizer is a spectrally broad and intense absorption band, a reversible electrochemical behavior, high stability under irradiation and the actual reaction conditions.[1,4,8,20] In this context, Cu^{I} complexes have recently been popularized as low-cost, noble metal-free systems.[1,2,4,8,9,12,15–17,19,21–25]

Recently, we reported a novel class of Cu^{I} complexes, namely homoleptic, anionic bis(4*H*-imidazolato)Cu^{I} cuprates.[26] This Cu^{I} complex class features an unprecedented broad and intense absorption spectrum ranging from the UV into the NIR region and exhibits low-energy metal-to-ligand charge-transfer (MLCT) transitions. The low-energy MLCT bands are due to the destabilization of the copper-based donor states by the two anionic 4*H*-imidazolate ligands and a stabilization of the ligand-based acceptor states.[26] Besides MLCT transitions, the main absorption band also contains ligand-centered (LC) bands. Computational investigations of the electronic properties of these homoleptic bis(4*H*-imidazolato)Cu^{I} complexes indicated the existence of just two acceptor orbitals (LUMO and LUMO + 1) for the NIR and visible transitions. These molecular orbitals are fully delocalized over both ligands. Detailed electrochemical investigations showed that the energy levels of the ligand-based electron acceptor states can be controlled by the substitution pattern of the *N*-aryl substituents while the energy levels of the copper-based oxidation states is controlled by the steric demand of the *N*-aryl substituents.[26]

[a] B. Seidler, J. H. Tran, J. Hniopek, P. Traber, Prof. Dr. S. Gräfe, Prof. Dr. M. Schmitt, Prof. Dr. J. Popp, Dr. M. Schulz, Prof. Dr. B. Dietzek-Ivanšić
Institute of Physical Chemistry
Friedrich Schiller University Jena
Helmholtzweg 4, 07743 Jena (Germany)
E-mail: martin.schulz.1@uni-jena.de
benjamin.dietzek@leibniz-ipht.de

[b] B. Seidler, J. Hniopek, Prof. Dr. J. Popp, Dr. M. Schulz, Prof. Dr. B. Dietzek-Ivanšić
Leibniz Institute of Photonic Technology Jena (Leibniz-IPHT)
Albert-Einstein-Str. 9, 07745 Jena (Germany)

[c] J. Hniopek, Prof. Dr. S. Gräfe, Prof. Dr. M. Schmitt, Prof. Dr. J. Popp, Prof. Dr. B. Dietzek-Ivanšić
Abbe Center of Photonics (ACP)
Albert-Einstein-Str. 6, 07745 Jena (Germany)

[d] Dr. H. Görls
Institute of Inorganic and Analytical Chemistry
Friedrich Schiller University Jena
Humboldtstr. 8, 07743 Jena (Germany)

[e] Prof. Dr. B. Dietzek-Ivanšić
Centre for Energy and Environmental Chemistry Jena (CEEC-Jena)
Friedrich Schiller University Jena
Philosophenweg 7a, 07743 Jena (Germany)

Supporting information for this article is available on the WWW under https://doi.org/10.1002/chem.202202697

In this study, we aimed to gain deeper insight into the electronic nature of the bis(4*H*-imidazolato)Cu^{I} complexes and their excited-state reactivity by femtosecond time-resolved transient absorption spectroscopy upon excitation into the LC and MLCT bands at 400, 480 and 630 nm and study the light-induced reactivity. The complexes Cu–F, Cu–Cl, and Cu–CF_3 (Figure 1) were selected due to the increasing electron-withdrawing properties of the *N*-aryl moieties.[26] Additionally, complex Cu–*2*CF_3 with increased steric demand was synthesized and studied. Our investigations reveal excited-state dynamics, which fundamentally differ from the related neutral, heteroleptic [Cu^{I}(xantphos)(4*H*-imidazolato)] complexes[27,28] as well as from homoleptic, cationic Cu^{I}bis(phenanthroline)- or Cu^{I}bis(bipyridine)-type complexes.[12,14,17,19,20,22,23,29]

Results and Discussion

Synthesis and characterization

The novel complex Cu–$2CF_3$ was synthesized according to previously established protocols.[26] Details can be found in the experimental section. Cu–$2CF_3$ was fully characterized by NMR spectroscopy, mass spectrometry, elemental analysis and X-ray diffraction. NMR investigations show that Cu–$2CF_3$ has a comparable charge distribution on the ligand as the already established complexes Cu–CF_3, Cu–Cl, and Cu–F, that is, a diminished electron density on the 4*H*-imidazolate core and increased electron density at the periphery.[26] The strong electron-withdrawing properties of the CF_3 groups facilitate the ligand-based electrochemical reduction (Figure S4A in the Supporting Information). Consequently, Cu–$2CF_3$ exhibits the least cathodic reduction potentials among the complexes studied here: −1.26, −1.55, and −1.96 V vs. Fc/Fc^{+} (cf. first reduction wave of: −1.43 V (Cu–CF_3), −1.70 V (Cu–F), −1.59 V (Cu–Cl) vs. Fc/Fc^{+}).[26] The copper-based oxidation reflects the increased steric demand, that is, the formation of a square planar coordination geometry upon Cu^{I}→Cu^{II} oxidation is hampered, and hence the oxidation potential is shifted to more positive potentials: +0.05 V (Figure S4B; Cu–$2CF_3$), −0.08 V (Cu–CF_3), −0.22 V (Cu–F), −0.17 V (Cu–Cl) vs. Fc/Fc^{+}.[26]

However, in the native Cu^{I} oxidation state of Cu–$2CF_3$, both ligands coordinate the copper center in a distorted tetrahedral fashion (single-crystal X-ray diffraction results; Figure S3), and hence the *N*-aryl rings can freely rotate. This is supported by ^{1}H and ^{13}C NMR spectroscopy, which features a single set of signals at room temperature (Figures S1 and S2).

Figure 2 presents the absorption spectra of all four Cu^{I} complexes dissolved in acetonitrile (ACN). The Cu^{I} complexes show an extremely broad absorption from 250 to 1100 nm, irrespective of the substitution pattern. In agreement with results from density functional theory (DFT) for Cu–F, Cu–Cl, and Cu–CF_3, the DFT calculations for Cu–$2CF_3$ (see Figures S27–S29 for details) reveal that the low-energy transitions in the NIR (S_1) and the absorption maximum (S_3, S_5, S_6) are mainly of MLCT character. The blue shoulder at 450 nm is attributed to an LC transition (S_{11}) as well as most of the transitions in the UV (S_{14}, S_{19}, S_{21}). For the complexes Cu–F and Cu–Cl, the bright MLCT transitions are S_1, S_3 and S_7. Also, transitions with mixed MLCT/LC character (S_4, S_{13}, S_{14}) and LC transitions (S_9, S_{10}), are found.[26] Based on these results the experimental absorptions in the NIR and low-energy flank of the absorption maximum are assigned to MLCT transitions while the blue flank of the absorption maximum is assigned to LC and mixed MLCT/LC transitions. Also, for Cu–$2CF_3$, only two acceptor MOs were found (LUMO and LUMO+1) independent of the nature of the optical transition. Both, the LUMO and the LUMO+1 are fully delocalized over both ligands (Figure S27).[26] UV/Vis−spectro-electrochemistry (UV/Vis-SEC) has proven valuable and experimentally supports the DFT assignment, as upon oxidation negative differential absorption in the region assigned to MLCT transitions appears for Cu–CF_3, Cu–Cl, and Cu–F.[26]

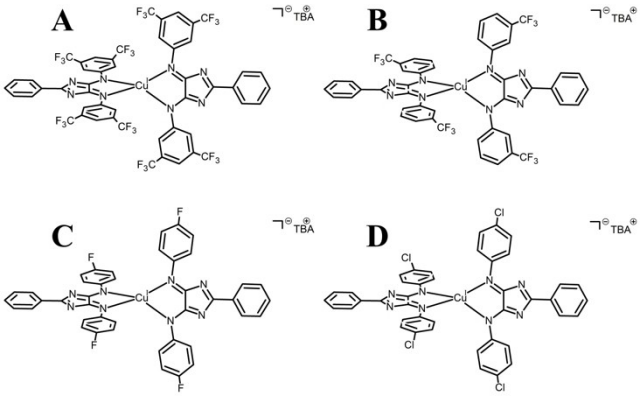

Figure 1. Chemical structure of the four different homoleptic bis(4*H*-imidazolato)Cu^{I} complexes A) Cu–$2CF_3$, B) Cu–CF_3, C) Cu–F, and D) Cu–Cl. Tetrabutylammonium (TBA) is the counter ion of all four complexes.

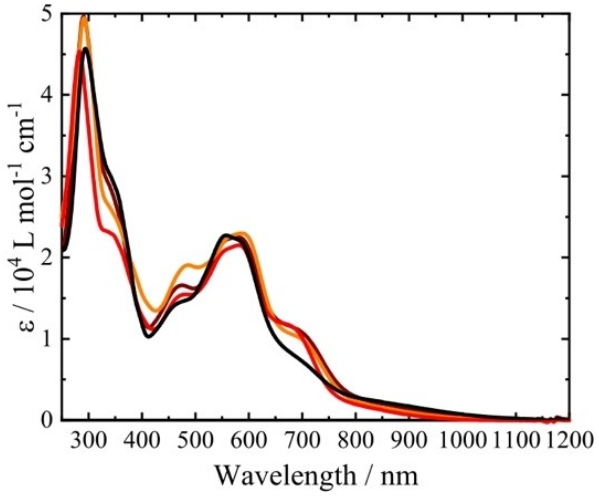

Figure 2. Steady-state absorption spectra of Cu–$2CF_3$ (black), Cu–CF_3 (brown), Cu–Cl (orange), and Cu–F (red) measured in ACN.

Ground-state absorption properties

UV/Vis-SEC experiments yield the absorption spectra of the oxidized and reduced species of Cu–2CF_3. Figure 3 shows the absorption difference spectra during reduction at a potential of −0.80 V as well as during oxidation at +0.90 V vs. Ag/AgCl as a reference electrode. During the reduction, positive signals occur in the region of 550 to 800 nm with a peak at 600 nm. The reduction events are assigned to be ligand-based.[25,30] For oxidation, positive peaks occur at 375 and 500 nm while a negative signal appears at 450 and 600 nm. The oxidation is correlated to the metal-based oxidation of copper.[25,30] UV/Vis-SEC data for all reductions and oxidation with the respective absorption spectra are shown in Figure S5. The combination of UV/Vis-SEC spectra of metal-based oxidation and ligand-based reduction is used to assign MLCT transitions in transient absorption experiments (see below).[2,28,31–34] While this approach relies on approximations, the UV/Vis-SEC data turned out to be the key to the interpretation of the transient absorption data discussed in the following section.

Excited-state absorption properties

To investigate the excited-state dynamics of the homoleptic bis(4*H*-imidazolato)Cu^{I} complexes, pump wavelength-dependent fs-TA spectra were recorded upon excitation at 400, 480 and 630 nm. Excitation at 400 nm populates mixed MLCT and LC states[26] while excitation at 480 nm populates also mixed states with more LC than MLCT character[26] (Figures S28 and S29). Excitation at 630 nm finally excites MLCT states (see Figures S28 and S29 for details).

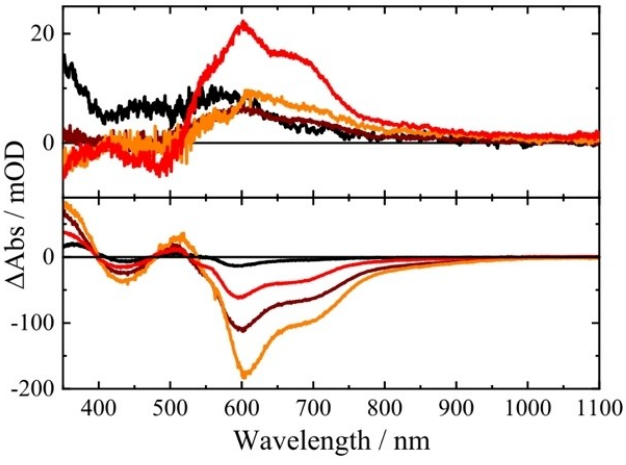

Figure 3. UV/Vis-SEC difference spectra of Cu–2CF_3 (black), Cu–CF_3 (brown), Cu–Cl (orange), and Cu–F (red) (UV/Vis-SEC data for Cu–CF_3, Cu–Cl, and Cu–F were previously published.[26]) for the first reduction at −0.53, −0.73, −0.90, −0.88 V vs. Ag/AgCl (top) and oxidation at +0.90, +0.85, +0.84, +0.85 V vs. Ag/AgCl (bottom) measured in 0.1 M $TBABF_4$ as supporting electrolyte in anhydrous and degassed ACN. The difference spectra were obtained by subtracting the open circuit potential (OCP) spectrum from the spectra of the reduced/oxidized species.

Figure 4 gives an overview on the results of the fs-TA measurements at the pump wavelength of 480 nm for Cu–2CF_3, Cu–CF_3, Cu–Cl, and Cu–F (top to bottom). At 300 fs after excitation, an excited-state absorption (ESA) at 400 nm with a small shoulder at 430 nm is accompanied by a ground-state bleach (GSB) in the region from 530 to 750 nm. The shape of the GSB with its two peaks at 600 and 700 nm matches the inverted ground-state absorption spectrum in the region between 600–750 nm of the non-emissive complexes. The deviation between the GSB and the inverted absorption spectrum in the region between 530–600 nm suggests a weak ESA contributing to the differential absorption signal below 530 nm. A more detailed perspective of the evolution of the TA spectra in the first 150 ps after excitation is given in Figure 5. Within 150 ps the TA signal decays to zero (Figure 4B) reflecting the short lifetime of the excited Cu^{I} complexes investigated here. Up to 4 ps after photoexcitation (Figure 5A) the minimum of the GSB signal shifts about 510 cm^{-1} from 583 to 601 nm (inset of Figure 5A). However, the negative differential absorption signal at around 700 nm does not shift spectrally nor decay in amplitude during such short delay times. This indicates that the shift of the GSB minimum in the range between 583 and 601 nm is due to an ESA overlapping with that GSB as reflected by the decay-associated spectra (DAS) at 0.7–1 ps (Figure 4C, F, I, L). In turn, we conclude that the ESA does not extend far beyond 600 nm, consequently leaving the negative differential absorption band at 700 nm unchanged. At longer delay times (Figure 5B) the shape of the GSB changes with increasing delay times as can particularly be seen between 550–600 nm as well as around 680 nm. This shape change is attributed to the change of the spectral profile of the overlapping ESA as reflected by the DAS at around 9 ps (Figure 4C,F,I,L). After that, the decay of the TA spectrum back to zero is observed.

In the following the observed spectral changes will be associated to the relevant time constants and discussed. In the discussion we will focus on the DAS as they reflect the spectral changes more clearly. To understand TA spectral changes (particularly when associated with a charge transfer), UV/Vis-SEC is a valuable tool. Thus, besides the transient absorption difference spectra, Figure 4 also depicts the combination of UV/Vis-SEC difference spectra recorded for the oxidation and first reduction event. To analyze the kinetics of the fs-TA data, 2D correlation analysis was applied following a recently established protocol (see page S14f in the Supporting Information and the Experimental Section for details).[35] Two-dimensional correlation analysis, in contrast to global lifetime analysis or methods such as multivariate curve resolution, offers a model and a priori information-free way to analyze TA data sets.

Thereby, it is possible to identify processes and estimate their characteristic timescales as well as their spectral responses, without enforcing a specific kinetic model or a predefined expected number of processes. The 2D correlation analysis yields equivalent data to decay-associated spectra (DAS) as well as an estimate of the respective time constants, which can be compared to results obtained from (conventional) global fitting using a sum of exponentials (Figure 4C, F, I, L). The time constants obtained from the three-exponential global fit routine

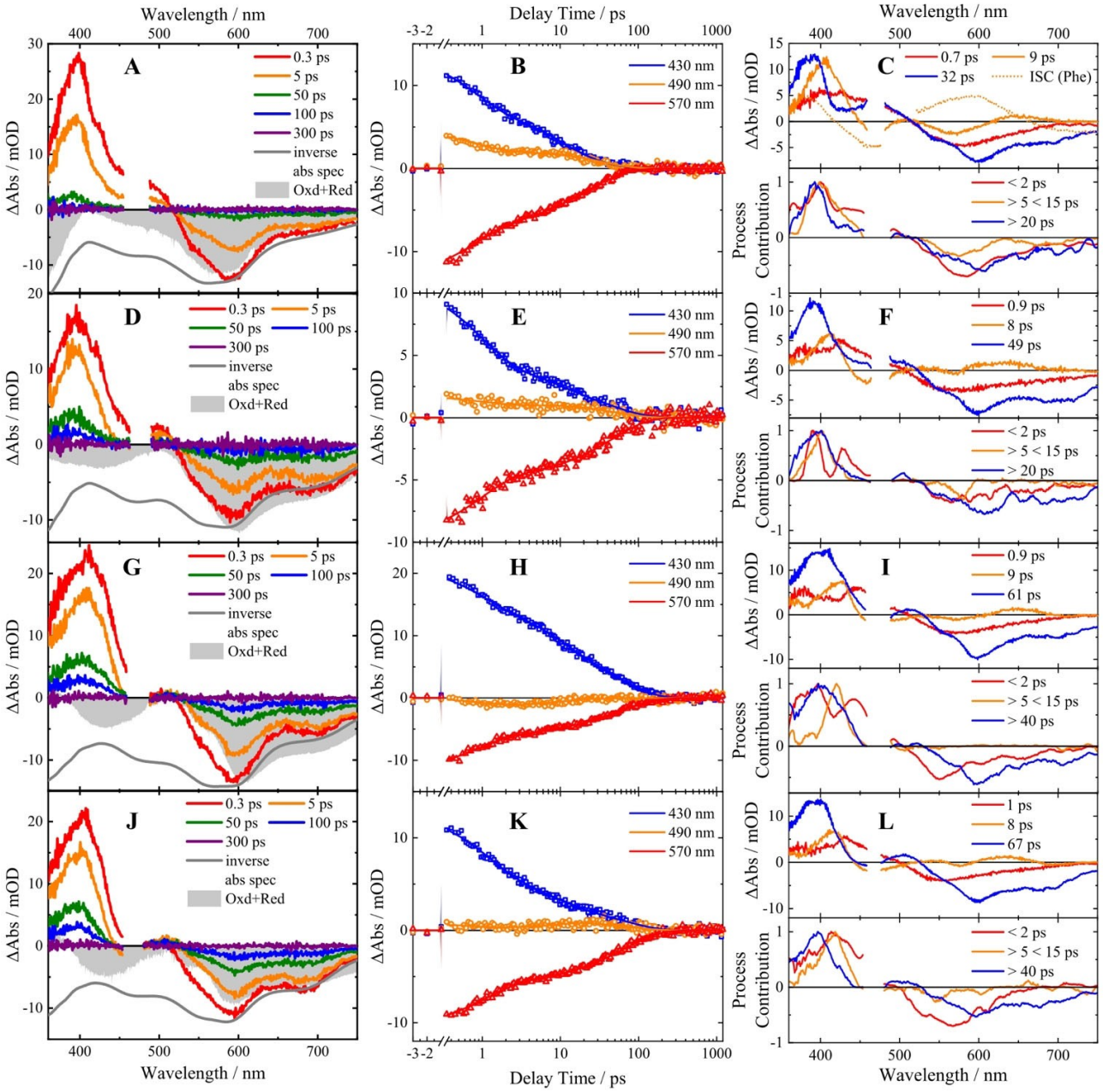

Figure 4. The temporal evolution of fs-TA spectra with a pump wavelength of 480 nm at different delay times is shown for A) Cu–2CF_3, D) Cu–CF_3, G) Cu–Cl, and J) Cu–F dissolved in ACN. Simulated MLCT absorption spectra[31] are shown in shaded gray and the inverted ground-state absorption spectra are shown as gray lines for comparison. B) Cu–2CF_3, E) Cu–CF_3, H) Cu–Cl and K) Cu–F display kinetic traces at selected probe wavelengths with a pump wavelength of 480 nm. The DAS for C) Cu–2CF_3, F) Cu–CF_3, I) Cu–Cl, and L) Cu–F with three time constants (τ_1, τ_2 and τ_3) were obtained from a three exponential fit routine (above) as well as a 2D correlation analysis (below). Furthermore, for Cu–2CF_3, the time constant related to ISC for a heteroleptic Cu^I complex (Phe) from previously published literature is also shown.[28]

are listed in Table S1. The time constants received from the 2D correlation are listed in Table S2. For an adequate description of the data obtained at 400, 480 and 630 nm pumps, three time constants were needed.

The three time constants, observed at 400, 480 and 630 nm pumps, respectively, are associated with very similar DAS and are denoted τ_1, τ_2, and τ_3. At all pump wavelengths, the DAS of time constant τ_1 (0.7–1 ps) is associated with a positive signal in the region from 380 to 500 nm and a negative signal in the region from 500 to 750 nm. These spectral changes are correlated to the decay of the ESA signal between 380 and 500 nm and the GSB signal from 530 to 750 nm in the TA data. The shape of the GSB matches the inverted absorption spectrum in the region between 600 and 750 nm (Figure 4A). However, a deviation between the GSB signal and the inverted absorption spectrum exists from 500 to 600 nm. This deviation suggests an ESA signal in this wavelength region. The small redshift in the GSB region (red line, Figure 4C, F, I, L and

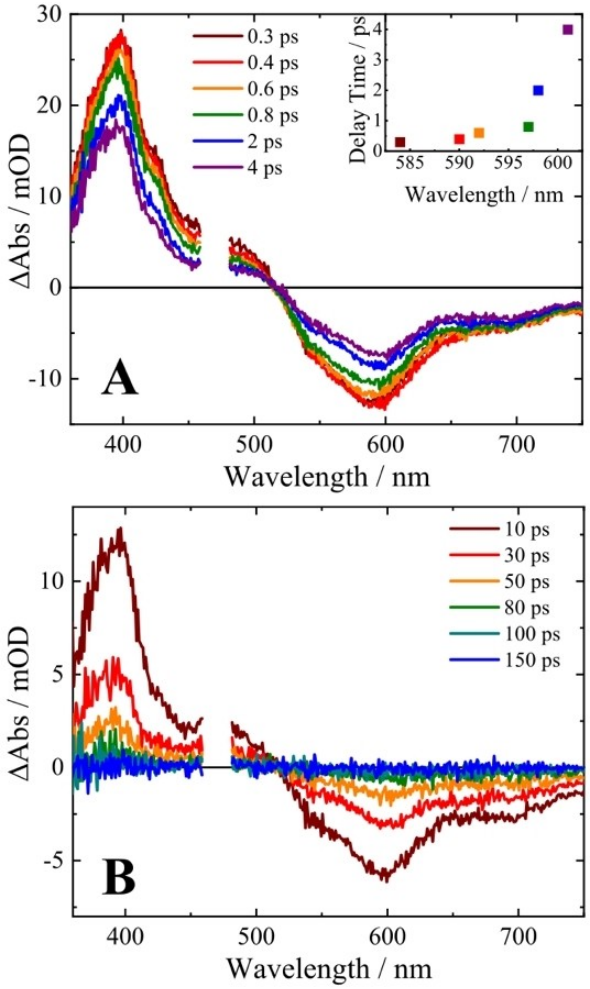

Figure 5. A) fs-TA spectra for Cu–$2CF_3$ upon excitation at 480 nm for short, selected delay times. The inset shows the red-shift of the GSB minimum with increasing delay time. B) This trend continues at longer delay times and is accompanied by a spectral shape change, particularly between 550–600 nm and around 680 nm.

Figure 5A inset) also originates from the suggested weak ESA in this region. A similar spectral signature is observed by 2D correlation analysis considering the data in the <2 ps delay-time window. To interpret the fs-TA data, a comparison with the UV/Vis-SEC data is helpful. Typically, the sum of the UV/Vis-SEC spectra of oxidation and first reduction match the spectral signature of MLCT states (see page S8 in the Supporting Information for details). In the data sets given in Figure 4, the TA data matches with the combined UV/Vis-SEC data only at long wavelengths, while there is a striking discrepancy in the shorter wavelength range. This mismatch stems from the fact that the acceptor orbitals of the optical transitions from the ground-state, which present the donor orbitals for excited-state absorptions, are fully delocalized over both ligands, while the absorptions of the singly reduced state (obtained electrochemically during UV/Vis-SEC) are localized on just one ligand.[26] The mismatch, however, does not indicate that the transition character is other than MLCT as established by TD-DFT results. Thus, τ_1 is interpreted as a re-localization of electron density from the delocalized Frank–Condon state into a localized state, rationalized by the similarity of the spectral signatures from the fs-TA experiment and that of the thermalized singly reduced species obtained by UV/Vis-SEC. Additionally, the pseudo-Jahn–Teller flattening distortion (PJT) from the distorted-tetrahedral FC geometry towards a square planar geometry typically takes place on the same timescale as τ_1 but is TA silent.[1,12,14,22–24] Therefore, both processes, re-localization and PJT occur in the sub-picosecond time window characterized by τ_1.

The DAS associated with τ_2 (~9 ps) features sharp positive signals at 400 and 650 nm. A negative signal appears at 460, 580 and 740 nm. These spectral changes reflect the decay of the ESA at 400 and 650 nm as well as an increase of the shoulder of the ESA at 460 nm and of the GSB at 580 nm along with a small redshift of the GSB.

The 2D correlation analysis in the delay-time range affected by τ_2 shows small changes in the differential absorption signal, that is, a positive signal at 400 nm and a negative signal between 500 to 780 nm. The slightly positive feature apparent in the DAS appears, if any, as a less-negative feature in the spectra determined by 2D correlation. Nonetheless, in the spectral range, in which stronger differential absorption signals are observed, both analyses yield consistent spectral features. The transient spectrum, which only becomes apparent from the appreciation of the DAS (as parts are cloaked by the strong GSB), is very similar to the transient spectrum of the heteroleptic [Cu^{I}(xantphos)(4*H*-imidazolato)] complexes[27,28] obtained after intersystem crossing (ISC) from the singlet to the triplet state. Due to these similarities the spectral changes associated with τ_2 are interpreted as ISC, which takes place after re-localization of the excited singlet state on one 4*H*-imidazolate ligands (τ_1). In contrast to the heteroleptic congeners, ISC occurs *after* the PJT relaxation, as also observed with comparable rate constants for bis(phenanthroline) or bis(bipyridine)-type complexes[1,11–13,22–24] due to smaller spin–orbit couplings (SOC) after PJT, that is, at relaxed geometries, compared to those at the Franck-Condon geometry.[17,28,36] Additionally, τ_2 follows the generally observed trend for Cu^{I} bisdiimine-type complexes, that electron-donating substituents lead to longer ISC time constants.[4,28]

The spectral changes, associated with τ_3 (32 to 67 ps) are a broad and pronounced positive signal in the region from 350 to 500 nm and a negative signal in the region from 500 to 750 nm. Furthermore, the 2D correlation analysis highlights the same spectral changes occurring in a delay-time window >40 ps. As no long-lived signal is observed, τ_3 is attributed to a ground-state recovery from the triplet into the singlet manifold.

The fs-TA data recorded upon excitation at 630 nm (Figure S7G–I) shows a similar behavior as for 480 nm excitation. Therefore, we assign the same processes as observed for 480 nm excitation. Excitation at 400 nm populates a mixture of MLCT and LC states, probably including also hot vibronic states. Experimentally, the shorter-wavelength excitation leads to quite similar spectral features compared to excitation at 480 and 630 nm (Figure 6; cf. kinetic traces at 430, 490 and 570 nm after

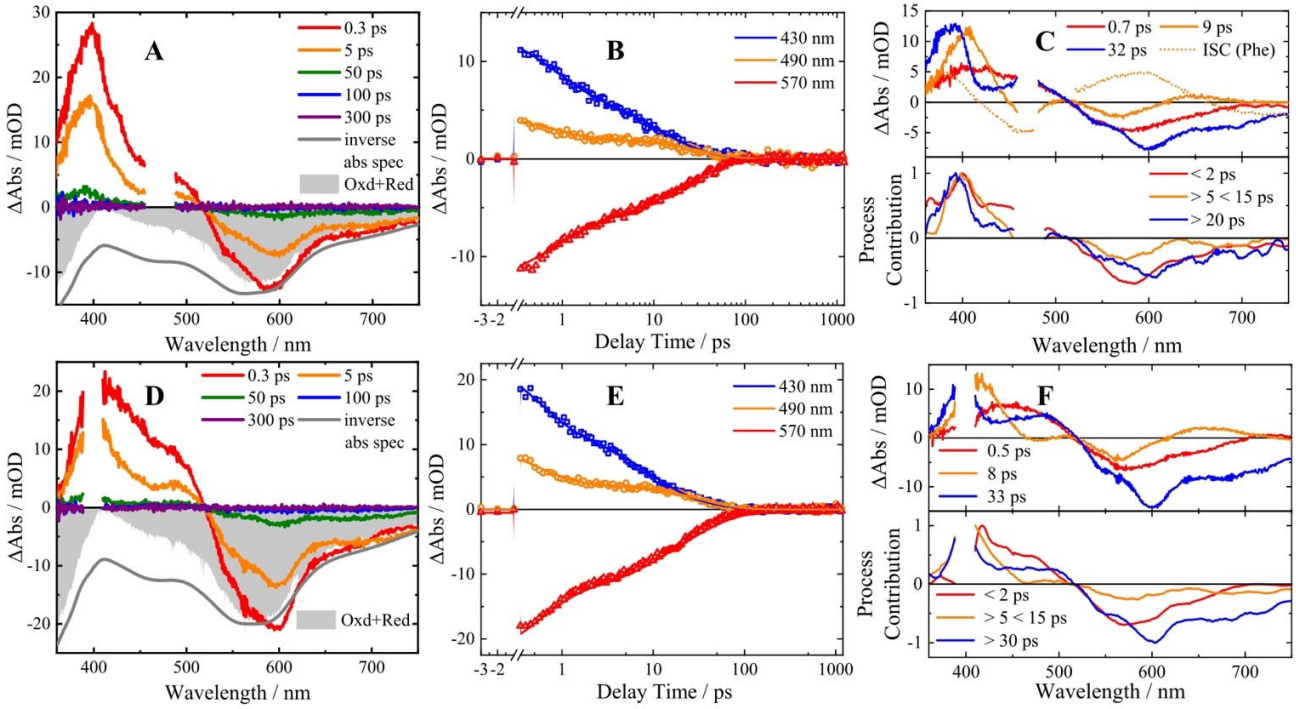

Figure 6. Temporal evolution of fs-TA spectra with a pump wavelength of A) 480 and D) 400 nm at different delay times for Cu–2CF$_3$ dissolved in ACN. Simulated MLCT absorption spectra[31] are shown in shaded gray and the inverted ground-state absorption spectra are shown as gray lines for comparison. Cu–2CF$_3$ shows kinetic traces at selected probe wavelengths with a pump wavelength of B) 480 and E) 400 nm. The DAS for Cu–2CF$_3$ upon pumping at C) 480 and F) 400 nm are given obtained from a three-exponential fit routine (above) and 2D correlation analysis (below).

excitation at 400 nm compared to excitation at 480 nm in Figure 6E and B). Figure 7 compares the kinetic traces recorded at 430, 490 and 570 nm, which reflect the very similar temporal evolution of the ESA and the GSB features, upon excitation at 400 and 480 nm. Though the 2D correlation analysis is especially sensitive to pulse overlap[35] spectra at delay times smaller than 500 fs were not considered. For all longer delay times, the spectral signatures and kinetic components observed for 400 nm excitation resemble those recorded upon excitation at 480 and 630 nm. Therefore, the excited-state dynamics associated with the characteristic time constants τ_1, τ_2 and τ_3 are pump wavelength independent.

The other investigated homoleptic Cu^{I} complexes Cu–CF$_3$, Cu–F and Cu–Cl (Figures S8, S9, and S10, respectively) show similar spectroscopic behavior as observed for Cu–2CF$_3$ irrespective of the particular pump wavelength. The time constants for the four homoleptic bis(4*H*-imidazolato)Cu^{I} complexes are listed in Table S1. Differences between the time constant τ_3 (Figure 8) were observed among the investigated complexes with the order Cu–2CF$_3$ < Cu–CF$_3$ < Cu–Cl ~ Cu–F, whereas the time constants for τ_1 and τ_2 are essentially unchanged.

Comparative theoretical calculations of Cu–2CF$_3$ and Cu–Cl reveal a relaxed triplet-state energy difference ΔE (electronic energy + thermal free energy correction) of 1.2 eV (Cu–2CF$_3$) and 0.7 eV (Cu–Cl) with respect to the singlet ground state.

Furthermore, a flattened geometry (small dihedral angle DHA between the N–Cu–N planes) is found for the Cu–2CF$_3$ singlet ground state (DHA 57°), which is very similar to the

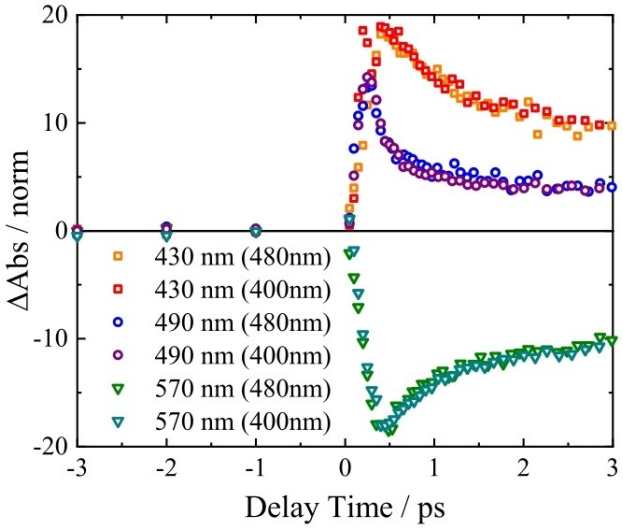

Figure 7. Comparison of kinetic traces for Cu–2CF$_3$ upon excitation at 400 and 480 nm for selected probe wavelengths (430, 490 and 570 nm) normalized to 0.45 ps to the kinetics of 400 nm displayed in the first 3 ps.

respective triplet-state geometry (DHA 59°). Cu–Cl in contrast only shows a flattened triplet state geometry (DHA 49°) and the expected pseudo-tetrahedral singlet ground state geometry (DHA 76°; Figure S31). We thus have Cu–2CF$_3$ with a larger S–T energy gap ΔE but little geometric distortion between singlet and triplet state along the DHA coordinate and with the

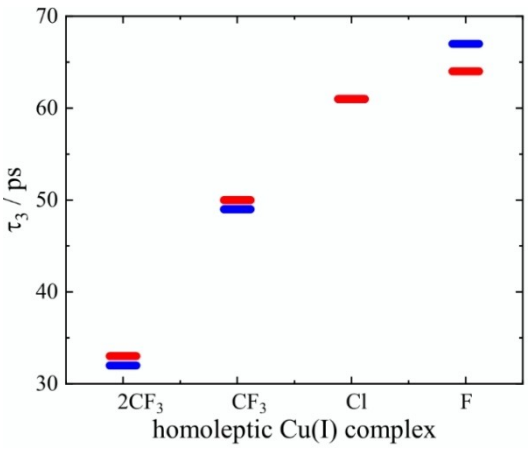

Figure 8. Comparison of the third time constant received from fs-TA data for all homoleptic Cu^{I} complexes. The third time constant is shown for excitation at 480 (blue) and 400 nm (red).

shortest decay time constant. And we have Cu–Cl with a very small ΔE but significant distortion along the DHA coordinate, yet a longer decay time constant. Note that the calculated dihedral angles are consistently smaller than those found by X-ray diffraction[26] (Figure S3) but reproduce the same trend.

The opposite trend of ΔE and τ_3 seems to contradict the energy gap law,[37] which is typically treated in the weak coupling limit for metal complexes (Figure S32). In the weak coupling limit, the energy gap law, relates the rate k_{nr} of the nonradiative decay to the energy difference between the potential energy minima of the two states involved, ΔE, as $k_{nr} \propto \exp(-\gamma \Delta E/\hbar\omega_M)$ whereby γ contains the relevant structural information on the relative displacement of the potential energy surfaces between the two electronic states and ω_M corresponds to the normal vibration of maximum frequency.[37] In the weak coupling limit, a minimal displacement between the potential energy minima along the reaction coordinate is assumed (Figure S32). On the basis of the theoretical results outlined above for Cu–Cl, considerable motion along the DHA coordinate must be considered and treatment of the decay in the strong coupling limit appears more suited. In the strong coupling limit, a substantial horizontal shift of the potential energy minima of the two electronic states along the reaction coordinate is considered. Now, the rate k_{nr} is no longer dependent on ΔE but mainly depends on E_A which represents the energy difference between the higher energy state minimum and the crossing point of the two potential energy parabola (Figure S32; $k_{nr} \propto \exp(-2E_A/\hbar < \omega >)$, with $< \omega >$ being the mean vibrational frequency).[37] We may thus conclude that the observed trend of τ_3 might have its origin in different decay mechanisms, which may be treated in the weak and strong coupling limit of the energy gap law, respectively. A quantitative treatment of the observed decay rates within the frame of the energy gap law and as detailed above is out of the scope of this work.

Conclusion

For the first time four homoleptic bis(4*H*-imidazolato)Cu^{I} complexes were studied with respect to their excited-state absorption properties by transient absorption spectroscopy. We compared the data obtained for different substitution patterns and pump wavelengths. Figure 9 summarizes the discussed photophysical model: the homoleptic bis(4*H*-imidazolato)Cu^{I} complexes populate fully delocalized excited-states of MLCT or mixed MLCT and LC character, upon excitation at 630, 480 and 400 nm. On a sub-1 ps timescale and independent of the pump wavelength, the excess electron density on the ligands is re-localized from a delocalized (over both ligands) to a localized state on a single 4*H*-imidazolate ligand and a fs-TA-silent PJT flattening distortion takes place. After re-localization of the electron density, ISC takes place in <10 ps. Finally, overall ground-state recovery from the triplet manifold on a fast timescale of only tens of picoseconds is observed. The short nonradiative decay time constants were rationalized by comparative DFT calculations revealing low triplet-state energies. Due to the considerable molecular motions, we suggest the treatment of the nonradiative decay within the strong coupling limit of the energy gap law.

The short excited-state lifetime precludes intermolecular excited energy or electron-transfer applications relying on diffusional encounter. But bis(4*H*-imidazolato) cuprates might still be attractive photosensitizers in systems through covalent bonding, for example, to fullerenes,[38] in molecular triads[39] or polyoxometalate dyads,[40] or by electrostatic interaction, which is under investigation. Moreover, specific alignment of the complexes might be a means to suppress nonradiative

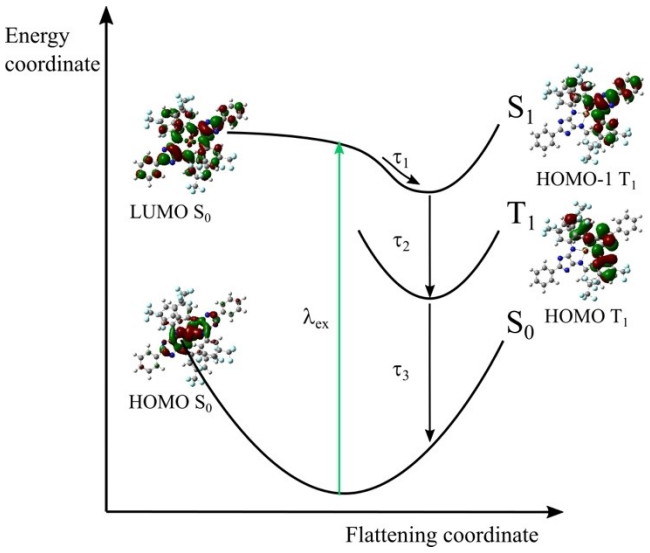

Figure 9. Model showing possible pathways for the excited states of homoleptic bis(4*H*-imidazolato)Cu^{I} complexes by photoexcitation. After photoexcitation a relocalization of electron density from a delocalized to a localized state appears ($\tau_1 = 0.7$–1 ps). Afterward, ISC ($\tau_2 = 6$–9 ps) and ground-state recovery ($\tau_3 = 30$–60 ps) occur. The following orbitals are graphically shown: HOMO S_0, LUMO S_0, HOMO T_1 and HOMO-1 T_1. Further information can be found in Figure S30.

decay.[41,42] In this regard the 4*H*-imidazole architecture offers a wide variety of substitution patterns.[43–45]

Experimental Section

Methods

NMR spectra were taken on a Bruker Advance III 400 MHz and 600 MHz spectrometer at a temperature of 20 °C. Tetramethylsilane (^{1}H and ^{13}C{1H} NMR) and trichlorofluoromethane (^{19}F NMR) were used as external standards and the spectrometer was locked to the residual solvent signal.

ESI-MS experiments were performed on a Bruker maXis. The experimental isotope pattern of the [M^+] peak was compared to the calculated isotope pattern.

Crystallographic data were collected on a Nonius KappaCCD diffractometer using graphite-monochromated $Mo_{K\alpha}$ radiation. Data were corrected for Lorentz and polarization effects; absorption was taken into account on a semi-empirical basis using multiple scans.[46–48] The structures were solved by direct methods (SHELXS[49]) and refined by full-matrix least-squares techniques against F_o^2 (SHELXL-2018[50]). All hydrogen atoms were included at calculated positions with fixed thermal parameters. All non-hydrogen atoms were refined anisotropically.[50] Disordered CF_3 groups were refined using bond lengths restraints and displacement parameter restraints. Some parts of the disorder model were introduced by the program DSR.[51] MERCURY[52] was used for structure representations.

UV/Vis absorption spectra were obtained in acetonitrile in a 1 cm quartz cuvette on a Jasco V-780 spectrometer at room temperature. The extinction coefficient was obtained through a dilution series at four concentrations, with absorbances in a range from 0.2 to 0.5. Solutions were prepared and filled in a glovebox under nitrogen.

Cyclic voltammetry was performed using a three-electrode setup with a glassy carbon working electrode, a platinum wire counter electrode and a Ag/Ag^+ wire pseudo-reference electrode. Samples were dissolved in 0.1 M $TBAPF_6$ in anhydrous ACN under nitrogen atmosphere. After the measurement ferrocene was added as an internal standard Fc/Fc^+.

UV/Vis-SEC experiments were performed with a VersaStat 3 potentiostat (Princeton Applied Research) with the software VersaStudio 2.49.2 using a three-electrode setup, with an ITO-coated PET film working electrode, a platinum wire counter electrode and a Ag/AgCl reference electrode. The samples were dissolved in 0.1 M $TBABF_4$ in anhydrous and degassed ACN in a SEC quartz cuvette with 2 mm optical pathlengths. Absorption spectra were taken with an AVANTES Multichannel Spectrometer with a deuterium and halogen lamp as light source (AvaLight-DH–S-BAL) controlled by the Avasoft8 software. The following procedure was used for all measurements: Firstly, the open circuit potential (OCP) was applied for 30 s and subsequently, the desired potential was applied for 5 min. Absorption spectra were taken prior to and after reaching the desired potential.

The fs-transient absorption setup as well as the procedure were already described elsewhere.[28,53] All fs-TA measurements were performed in anhydrous and degassed acetonitrile solution in 1 mm quartz cuvettes with an optical density between 0.3 and 0.4 at the respective pump wavelength. The probe pulse was generated in a calcium fluoride crystal with a pulse energy of 25 nJ. The applied pump power at each pump wavelengths (400, 480 and 630 nm) was 0.45 mW. To ensure reproducibility all samples were independently measured three times. The integrity of the samples was checked by absorption measurements before and after each fs-TA experiment on a JASCO V530 UV/Vis spectrometer.

2D correlation spectroscopy of the transient absorption spectra (TA-2DCOS) was detailly described elsewhere.[35] Briefly, the analyses were conducted in GNU R, version 4.0.2.[54] All raw spectra were pre-processed by removing values for delay times smaller than 500 fs (TA-2DCOS is especially sensitive to pulse overlap),[35] and smoothing using a third order Savitzky-Golay filter with a width of 29 spectral variables. Afterwards, the data sets were sliced into time-delay windows of 10 spectra each and the TA-2DCOS routine was applied. Relevant windows for further analysis were selected using the total correlation intensity approach described in ref. [35]. The resulting TA-2DCOS contour spectra can be found in Figures S15–S26. To extract the process associated spectral profiles, the Pearson correlation matrix of each window was calculated and used to afford strictly linear 2DCOS maps.[35] Slice spectra, corresponding to the peak centers of significant correlation signals observed in the correlation maps (Figures S15–S26) were selected to extract the spectral profiles. The spectral profiles were subsequently unit scaled and their sign was corrected by calculating the absolute change of intensity of the slice in the respective window. These profiles are displayed in Figures S11–S14.

All calculations were performed with Gaussian 16 Rev. B.01.[55] The hybrid exchange correlation functional PBE0 in combination with the double-ζ basis set def2-SV(P)[56] and its corresponding electronic core potential was used for all calculations. All geometry optimizations were performed using Gaussian's tight threshold. To account for dispersion interactions, Grimme's D3 correction was applied in the Becke–Johnson damping version.[57] The solvent environment was included implicitly using the integral equation formalism variant of the polarizable continuum model (IEF-PCM)[58–60] for acetonitrile ($\varepsilon = 35.688$, $n = \varepsilon(\infty) = 1.806874$). Minimum geometries were verified to be local minima on the potential energy hypersurface by a normal mode analysis. Frequency and excitation calculations were performed without symmetry constraints using the optimized ground-state geometries. Within the TD-DFT calculations, the first 100 excited singlet transitions were taken into account. The character of the respective transitions was assigned on the basis of the percent contributions of the involved molecular orbitals (MOs) using TheoDORE 2.1.[61–66] and plotted at an isovalue = 0.0004.

Experimental data

Materials: Chemicals were obtained from Carl Roth in synthesis grade quality, if not mentioned otherwise, and were used without further purifications. THF and toluene were dried over sodium, for acetonitrile (ACN) and dichloromethane (DCM) calcium hydride was used as a drying agent. Amberlyst A21 (Alfa Aesar) was washed with dichloromethane before use. Tetrabutylammonium fluoride (TBAF), was obtained from Sigma–Aldrich and used as 1 M solution in THF.

Synthesis: The ligand Hlm (0.2 mmol, 2 equiv.) was suspended in 25 mL ACN together with 1 g of Amberlyst A21. The suspension was stirred at room temperature for 14 h. Subsequently [Cu(acetonitrilo)$_4$]PF_6 (0.1 mmol, 1 equiv.) was added to the solution. After 4 h of stirring at room temperature the solution was filtered and the remaining Amberlyst A21 beads were washed three times with a total of 15 mL ACN and dried in vacuo. $TBAF \cdot 3H_2O$ (0.12 mmol, 1.2 equiv.) dissolved in 50 mL THF was added to the Amberlyst A21 beads and stirred for 18 h at room temperature. The Amberlyst A21 beads were separated from the THF solution and subsequently washed three times with a total of 10 mL THF.

Removal of the solvent from the combined THF solutions furnished a deep blue solid, which was dried in vacuo. The crude product was purified by column chromatography with ACN/toluene (1:3, *v/v*) on basic alumina. Single crystals were received from an ACN/toluene mixture by slow evaporation of the solvent.

Tetrabutylammonium bis((3,5-bis(trifluormethane)-phenyl)4-(3,5-bis(trifluormethane)phenyl)-imino-κN-2-phenyl-4*H*-imidazol-5-ylamido-κN) cuprate(I) (Cu–*2CF*$_3$): Yield: 423.5 mg (67%). ^{1}H NMR (CD_2Cl_2; 400 MHz):δ = 8.68 (s, 8H, *o*-CH^{N-Ar}), 8.60–8.65 (m, 4H, *o*-CH^{2-Ph}), 7.66 (t, J = 7.6 Hz, 2H, *p*-CH^{2-Ph}), 7.56 (t, J = 7.6 Hz, 4H, *m*-CH^{2-Ph}), 7.50 (s, 4H, *p*-CH^{N-Ar}), 2.88–2.97 (m, 8H, CH_2^{TBA}), 2.86–3.00 (m, 8H), 1.25–1.39 (m, 1H, CH_2^{TBA}), 0.94 ppm (t, J = 7.3 Hz, 12H, CH_3^{TBA}). ^{13}C NMR (CD_2Cl_2; 101 MHz): δ = 191.0 ($C2^{Im}$), 172.8 ($C4,5^{Im}$), 149.2 (*ipso*-C^{N-Ar}), 134.5 (*ipso*-C^{2-Ph}), 133.4 (*p*-CH^{2-Ph}), 131.93 ($^2J_{C,F}$ = 33.76 Hz, CCF_3^{N-Ar}), 130.6 (*o*-CH^{2-Ph}),129.1 (*m*-CH^{2-Ph}), 126.9 (*o*-CH^{N-Ar}), 124,11 ($^1J_{C,F}$ = 272.42 Hz, CF_3^{N-Ar}), 118.3 ($^3J_{C,F}$ = 3.45 Hz, *p*-CH^{N-Ar}), 59.5 (CH_2^{TBA}), 24.3 (CH_2^{TBA}), 20.1 (CH_2^{TBA}), 13.7 ppm (CH_3^{TBA}). ^{19}F NMR (CD_2Cl_2; 377 MHz): δ = 63 ppm MS (ESI, pos.): m/z (%) = 242 $[TBA]^+$ (100); 186 $[NHBu_3]^+$ (3). MS (ESI, neg.): m/z (%) = 1253 $[Cu(Im–CF_3)_2]^-$ (100); 595 (9) $[Im–CF_3]^+$. Elemental analysis calcd (%) for $C_{66}H_{58}CuF_{24}N_9 + {}^1/_3C_7H_8$: C 53.75, H 4.21, N 8.11; found: C 53.73, H 4.00, N 8.25.

Deposition Number 1995044 (for Cu–2CF_3) contains the supplementary crystallographic data for this paper. These data are provided free of charge by the joint Cambridge Crystallographic Data Centre and Fachinformationszentrum Karlsruhe Access Structures service.

Supporting Information

NMR-spectra, X-ray diffraction details, electrochemistry data (CV, UV/Vis-SEC), fs-TA data of all complexes at the different excitation wavelengths, 2D correlation details and data as well as computational results are given.

Acknowledgements

The authors gratefully acknowledge support from the Deutsche Forschungsgemeinschaft (DFG, German Research Foundation) Projektnummer 364549901-TRR 234 "CataLight". Open Access funding enabled and organized by Projekt DEAL.

Conflict of Interest

The authors declare no conflict of interest.

Data Availability Statement

The data that support the findings of this study are available in the supplementary material of this article.

Keywords: absorption · copper complexes · cyclic voltammetry · photophysics · time-resolved spectroscopy

[1] M. Sandroni, Y. Pellegrin, F. Odobel, *Comptes Rendus Chim.* **2016**, *19*, 79–93.
[2] Y. Zhang, L. Zedler, M. Karnahl, B. Dietzek, *Phys. Chem. Chem. Phys.* **2019**, *21*, 10716–10725.
[3] Y. Zhang, M. Heberle, M. Wächtler, M. Karnahl, B. Dietzek, M. Waechtler, M. Karnahl, B. Dietzek, *RSC Adv.* **2016**, *6*, 105801–105805.
[4] S. Tschierlei, M. Karnahl, N. Rockstroh, H. Junge, M. Beller, S. Lochbrunner, *ChemPhysChem* **2014**, *15*, 3709–3713.
[5] S. Fischer, D. Hollmann, S. Tschierlei, M. Karnahl, N. Rockstroh, E. Barsch, P. Schwarzbach, S.-P. Luo, H. Junge, M. Beller, et al., *ACS Catal.* **2014**, *4*, 1845–1849.
[6] M. Karnahl, E. Mejía, N. Rockstroh, S. Tschierlei, S.-P. Luo, K. Grabow, A. Kruth, V. Brüser, H. Junge, S. Lochbrunner, et al., *ChemCatChem* **2014**, *6*, 82–86.
[7] M. Heberle, S. Tschierlei, N. Rockstroh, M. Ringenberg, W. Frey, H. Junge, M. Beller, S. Lochbrunner, M. Karnahl, *Chem. Eur. J.* **2017**, *23*, 312–319.
[8] M.-A. Schmid, M. Rentschler, W. Frey, S. Tschierlei, M. Karnahl, *Inorganics* **2018**, *6*, 134.
[9] E. Mejía, S.-P. Luo, M. Karnahl, A. Friedrich, S. Tschierlei, A.-E. Surkus, H. Junge, S. Gladiali, S. Lochbrunner, M. Beller, *Chem. Eur. J.* **2013**, *19*, 15972–15978.
[10] L. X. Chen, G. B. Shaw, I. Novozhilova, T. Liu, G. Jennings, K. Attenkofer, G. J. Meyer, P. Coppens, *J. Am. Chem. Soc.* **2003**, *125*, 7022–7034.
[11] J. V. Lockard, S. Kabehie, J. I. Zink, G. Smolentsev, A. Soldatov, L. X. Chen, *J. Phys. Chem. B* **2010**, *114*, 14521–14527.
[12] N. A. Gothard, M. W. Mara, J. Huang, J. M. Szarko, B. Rolczynski, J. V. Lockard, L. X. Chen, *J. Phys. Chem. A* **2012**, *116*, 1984–1992.
[13] G. B. Shaw, C. D. Grant, H. Shirota, E. W. Castner, G. J. Meyer, L. X. Chen, *J. Am. Chem. Soc.* **2007**, *129*, 2147–2160.
[14] M. W. Mara, N. E. Jackson, J. Huang, A. B. Stickrath, X. Zhang, N. A. Gothard, M. A. Ratner, L. X. Chen, *J. Phys. Chem. B* **2013**, *117*, 1921–1931.
[15] R. Fayad, S. Engl, E. O. Danilov, C. E. Hauke, O. Reiser, F. N. Castellano, *J. Phys. Chem. Lett.* **2020**, *11*, 5345–5349.
[16] Y. Zhang, P. Traber, L. Zedler, S. Kupfer, S. Gräfe, M. Schulz, W. Frey, M. Karnahl, B. Dietzek, *Phys. Chem. Chem. Phys.* **2018**, *20*, 24843–24857.
[17] Z. A. Siddique, Y. Yamamoto, T. Ohno, K. Nozaki, *Inorg. Chem.* **2003**, *42*, 6366–6378.
[18] C. Müller, M. Schulz, M. Obst, L. Zedler, S. Gräfe, S. Kupfer, B. Dietzek, *J. Phys. Chem. A* **2020**, *124*, 6607–6616.
[19] Y. Zhang, M. Schulz, M. Wächtler, M. Karnahl, B. Dietzek, *Coord. Chem. Rev.* **2018**, *356*, 127–146.
[20] V. Leandri, A. R. P. Pizzichetti, B. Xu, D. Franchi, W. Zhang, I. Benesperi, M. Freitag, L. Sun, L. Kloo, J. M. Gardner, *Inorg. Chem.* **2019**, *58*, 12167–12177.
[21] X. L. Chen, R. Yu, Q. K. Zhang, L. J. Zhou, X. Y. Wu, Q. Zhang, C. Z. Lu, *Chem. Mater.* **2013**, *25*, 3910–3920.
[22] M. Iwamura, S. Takeuchi, T. Tahara, *Acc. Chem. Res.* **2015**, *48*, 782–791.
[23] S. Garakyaraghi, E. O. Danilov, C. E. McCusker, F. N. Castellano, *J. Phys. Chem. A* **2015**, *119*, 3181–3193.
[24] M. W. Mara, K. A. Fransted, L. X. Chen, *Coord. Chem. Rev.* **2015**, *282–283*, 2–18.
[25] M. Schulz, N. Hagmeyer, F. Wehmeyer, G. Lowe, M. Rosenkranz, B. Seidler, A. Popov, C. Streb, J. G. Vos, B. Dietzek, *J. Am. Chem. Soc.* **2020**, *142*, 15722–15728.
[26] J. H. Tran, P. Traber, B. Seidler, H. Görls, S. Gräfe, M. Schulz, *Chem. Eur. J.* **2022**, *28*, e202200121.
[27] M. Schulz, C. Reichardt, C. Müller, K. R. A. Schneider, J. Holste, B. Dietzek, *Inorg. Chem.* **2017**, *56*, 12978–12986.
[28] B. Seidler, M. Sittig, C. Zens, J. H. Tran, C. Müller, Y. Zhang, K. R. A. Schneider, H. Görls, A. Schubert, S. Gräfe, et al., *J. Phys. Chem. B* **2021**, *125*, 11498–11511.
[29] J. R. Kirchhoff, D. R. McMillin, W. R. Robinson, D. R. Powell, A. T. McKenzie, S. Chen, *Inorg. Chem.* **1985**, *24*, 3928–3933.
[30] M. Schulz, F. Dröge, F. Herrmann-Westendorf, J. Schindler, H. Görls, M. Presselt, *Dalton Trans.* **2016**, *45*, 4835–4842.
[31] A. M. Brown, C. E. McCusker, J. K. McCusker, *Dalton Trans.* **2014**, *43*, 17635–17646.
[32] S. Bold, L. Zedler, Y. Zhang, J. Massin, V. Artero, M. Chavarot-Kerlidou, B. Dietzek, *Chem. Commun.* **2018**, *54*, 10594–10597.
[33] R. M. Berger, *Inorg. Chem.* **1990**, *29*, 1920–1924.
[34] D. Kuciauskas, J. E. Monat, R. Villahermosa, H. B. Gray, N. S. Lewis, J. K. McCusker, *J. Phys. Chem. B* **2002**, *106*, 9347–9358.
[35] J. Hniopek, C. Müller, T. Bocklitz, M. Schmitt, B. Dietzek, J. Popp, *J. Phys. Chem. Lett.* **2021**, *12*, 4148–4153.

[36] P. C. J. Kamer, P. W. N. M. Van Leeuwen, J. N. H. Reek, *Acc. Chem. Res.* **2001**, *34*, 895–904.
[37] R. Englman, J. Jortner, *Mol. Phys.* **1970**, *18*, 145–164.
[38] S. Fukuzumi, K. Ohkubo, H. Imahori, D. M. Guldi, *Chem. Eur. J.* **2003**, *9*, 1585–1593.
[39] Y. Luo, K. Barthelmes, M. Wächtler, A. Winter, U. S. Schubert, B. Dietzek, *Chem. Eur. J.* **2017**, *23*, 4917–4922.
[40] Y. Luo, S. Maloul, S. Schönweiz, M. Wächtler, C. Streb, B. Dietzek, *Chem. Eur. J.* **2020**, *26*, 8045–8052.
[41] J. A. Treadway, B. Loeb, R. Lopez, P. A. Anderson, F. R. Keene, T. J. Meyer, *Inorg. Chem.* **1996**, *35*, 2242–2246.
[42] Y. C. Wei, S. F. Wang, Y. Hu, L. S. Liao, D. G. Chen, K. H. Chang, C. W. Wang, S. H. Liu, W. H. Chan, J. L. Liao, et al., *Nat. Photonics* **2020**, *14*, 570–577.
[43] J. Blumhoff, R. Beckert, S. Rau, S. Losse, M. Matschke, W. Günther, H. Görls, *Eur. J. Inorg. Chem.* **2009**, *2009*, 2162–2169.
[44] J. Fabian, H. Görls, R. Beckert, J. Atzrodt, *J. Prakt. Chem.* **1997**, *339*, 735–741.
[45] J. Atzrodt, R. Beckert, H. Görls, *Heterocycles* **1999**, *51*, 763.
[46] COLLECT, Data Collection Software; Nonius B.V., Netherlands, **1998**.
[47] Z. Otwinowski, W. Minor in Methods Enzymology, *Vol. 276: Macromolecular Crystallography*, *Part A* (Eds.: C. W. Carter, R. M. Sweet), Academic Press, **1997**, pp. 307–326.
[48] L. Krause, R. Herbst-Irmer, G. M. Sheldrick, D. Stalke, *J. Appl. Crystallogr.* **2015**, *48*, 3–10.
[49] G. M. Sheldrick, *Acta Crystallogr. Sect. A* **2008**, *64*, 112–122.
[50] G. M. Sheldrick, *Acta Crystallogr. Sect. A* **2015**, *71*, 3–8.
[51] D. Kratzert, I. Krossing, *J. Appl. Crystallogr.* **2018**, *51*, 928–934.
[52] C. F. Macrae, P. R. Edgington, P. McCabe, E. Pidcock, G. P. Shields, R. Taylor, M. Towler, J. van de Streek, *J. Appl. Crystallogr.* **2006**, *39*, 453–457.
[53] M. Karnahl, C. Kuhnt, F. Ma, A. Yartsev, M. Schmitt, B. Dietzek, S. Rau, J. Popp, *ChemPhysChem* **2011**, *12*, 2101–2109.
[54] R: A Language and Environment for Statistical Computing, R Foundation for Statistical Computing, R Core Team, Vienna Austria, **2020**.
[55] M. J. Frisch, G. W. Trucks, H. B. Schlegel, G. E. Scuseria, M. A. Robb, J. R. Cheeseman, G. Scalmani, V. Barone, G. A. Petersson, H. Nakatsuji, et al., **2016**, Gaussian 16, Revision C.01, Gaussian, Inc., Wallin.
[56] C. Adamo, V. Barone, *J. Chem. Phys.* **1999**, *110*, 6158–6170.
[57] S. Grimme, S. Ehrlich, L. Goerigk, *J. Comput. Chem.* **2011**, *32*, 1456–1465.
[58] E. Cancès, B. Mennucci, J. Tomasi, *J. Chem. Phys.* **1997**, *107*, 3032–3041.
[59] E. Cancès, B. Mennucci, *J. Math. Chem.* **1998**, *23*, 309–326.
[60] J. Tomasi, B. Mennucci, R. Cammi, *Chem. Rev.* **2005**, *105*, 2999–3094.
[61] F. Plasser, *J. Chem. Phys.* **2020**, *152*, 084108.
[62] F. Plasser, *J. Chem. Phys.* **2016**, *144*, 194107.
[63] S. A. Mewes, F. Plasser, A. Dreuw, *J. Chem. Phys.* **2015**, *143*, 171101.
[64] S. A. Bäppler, F. Plasser, M. Wormit, A. Dreuw, *Phys. Rev. A* **2014**, *90*, 052521.
[65] F. Plasser, M. Wormit, A. Dreuw, *J. Chem. Phys.* **2014**, *141*, 024106.
[66] F. Plasser, H. Lischka, *J. Chem. Theory Comput.* **2012**, *8*, 2777–2789.

Manuscript received: August 29, 2022
Accepted manuscript online: September 23, 2022
Version of record online: October 31, 2022